Solute tracer test quantification of the effects of hot water injection into hydraulically stimulated crystalline rock

Journal Article

Author(s):
Kittilä, Anniina; Jalali, Mohammadreza; Saar, Martin O.; Kong, Xiang-Zhao (iD)

RESEARCH

Solute tracer test quantification of the effects of hot water injection into hydraulically stimulated crystalline rock

Anniina Kittilä[1,5], Mohammadreza Jalali[2,3], Martin O. Saar[1,4] and Xiang-Zhao Kong[1]*

*Correspondence:
xkong@ethz.ch
[1] Geothermal Energy
and Geofluids Group,
Department of Earth
Sciences, ETH Zürich,
Sonneggstrasse 5,
Zürich 8092, Switzerland
Full list of author information
is available at the end of the
article

Abstract

When water is injected into a fracture-dominated reservoir that is cooler or hotter than the injected water, the reservoir permeability is expected to be altered by the injection-induced thermo-mechanical effects, resulting in the redistribution of fluid flow in the reservoir. These effects are important to be taken into account when evaluating the performance and lifetime particularly of Enhanced Geothermal Systems (EGS). In this paper, we compare the results from two dye tracer tests, conducted before (at ambient temperature of 13 °C) and during the injection of 45 °C hot water into a fractured crystalline rock at the Grimsel Test Site in Switzerland. Conducting a moment analysis on the recovered tracer residence time distribution (RTD) curves, we observe, after hot water injection, a significant decrease in the total tracer recovery. This recovery decrease strongly suggests that fluid flow was redistributed in the studied rock volume and that the majority of the injected water was lost to the far-field. Furthermore, using temperature measurements, obtained from the same locations as the tracer RTD curves, we conceptualize an approach to estimate the fracture surface area contributing to the heat exchange between the host rock and the circulating fluid. Our moment analysis and simplified estimation of fracture surface area provide insights into the hydraulic properties of the hydraulically active fracture system and the changes in fluid flow. Such insights are important to assess the heat exchange performance of a geothermal formation during fluid circulation and to estimate the lifetime of the geothermal formation, particularly in EGS.

Keywords: Geothermal energy, Tracer test, Moment analysis, Hot water injection, Hydraulic stimulation, Crystalline rock, Fractured reservoirs

Introduction

To produce energy from geothermal resources, fluid is injected and circulated through natural or artificially created reservoirs, the latter being so-called enhanced/engineered geothermal systems (EGS) (Tester et al. 2006; Evans 2015). As the fluid flows through the natural or artificial reservoir, heat is exchanged between the host rock and the circulating fluid. The performance of a geothermal system, in terms of fluid circulation and heat extraction, depends on several factors, where the reservoir impedance, the heat recovery, and the tracer-swept volume are key factors (Tester et al. 2006; Grant 2016; Olasolo

Kittilä *et al. Geotherm Energy*   (2020) 8:17

Page 2 of 21

et al. 2016). The larger the heat exchange surface area between the fluid and the rock, the better the geothermal resource can be exploited and the longer is the expected lifetime of the reservoir before cold-front breakthrough occurs at the production well. However, thermo-hydro-mechanical–chemical responses of the formation can have detrimental effects on the performance of a geothermal reservoir (André et al. 2006; Taron and Elsworth 2009; Fu et al. 2016; Pandey et al. 2017).

Whenever the temperature of the injected fluid is different to the one of the reservoir, particularly in crystalline, fractured rock, it is likely that thermal, mechanical, and chemical processes alter the hydraulic properties of the rock mass. It has been reported that both heat extraction and heat storage in fractured reservoirs can cause rock deformation, inducing changes in fracture aperture widths (Fu et al. 2016; Pandey et al. 2017). In fracture-dominated systems, such as EGS, heat production, by injecting water that is cooler than the natural rock, eventually results in flow channeling, i.e., concentration of fluid flow in cooled zones (Fu et al. 2016). In a heating experiment reported by Rutqvist et al. (2001), elevated fluid temperatures caused the surrounding rock to expand, yielding vertical rock displacement. Kumari et al. (2018) conducted flow-through experiments in a granite core under different temperature conditions and demonstrated that increasing the temperature of the injected fluid from 20 to 300 °C, caused an 86% reduction in permeability before reaching 100 °C. Recently, Grimm Lima et al. (2019) observed a 20–75% decrease in the hydraulic apertures of naturally fractured granodiorite cores from the Grimsel Test Site (GTS) in Switzerland (which is also the field site in this paper), when increasing the temperature of the system from 22 to 140 °C. Kumari et al. (2018) and Grimm Lima et al. (2019) identified that the reductions in permeability and in fracture apertures as well as the closure of fractures are caused by the thermal expansion of the rock. Moreover, Grimm Lima et al. (2019) demonstrated pressure dissolution of contacting asperities.

Although the injection of heat induces the aforementioned thermo-mechanical effects, heat is a well-established tracer in the subsurface both as a natural (Saar et al. 2011) and an artificially introduced tracer, with typical applications in reservoir characterization (Colombani et al. 2015; Irvine et al. 2015; Ayling et al. 2016; Sarris et al. 2018) and tomography (Linde et al. 2006; Somogyvári et al. 2016; Somogyvári and Bayer 2017). Heat can be a valuable tool in acquiring additional information on subsurface fluid flow and (solute, energy) transport processes, particularly when estimating permeability (McCord et al. 1992; Anderson 2005). However, the solute and thermal Peclet numbers can differ by orders of magnitude for the same Darcy flow velocity (de Marsily 1986), which can cause problems, for example, when solute transport is of interest but only heat is used as a tracer. This discrepancy between solute and heat transport is particularly severe in fine-grained sediments, as heat transport is relatively insensitive to changes in longitudinal dispersivity, which is a particularly relevant parameter for solute transport modeling (Rau et al. 2012; Giambastiani et al. 2013). Notwithstanding these differences, Marschall et al. (1995) used solutes and heat to investigate the role of diffusive transport in a fractured rock. However, in that experiment the thermal expansion of the rock was not considered, although an increase in injection pressure and a decrease in injection flow rate were observed. The study of Kumari et al. (2018), on the other hand, considered the temperature effect on permeability during water injection at

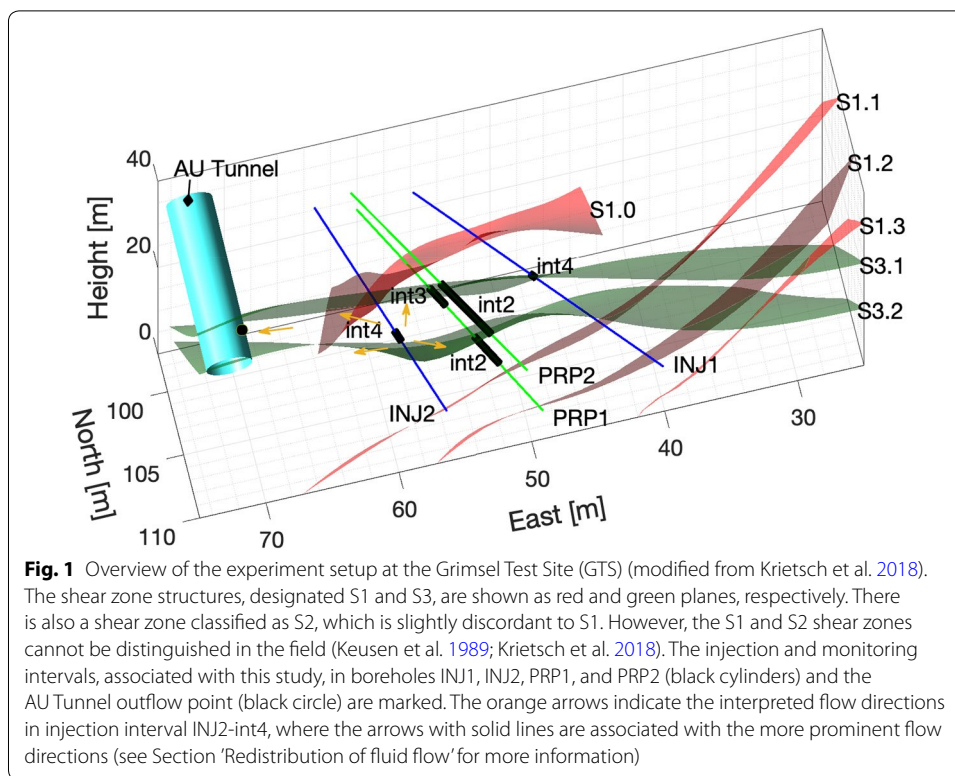Kittilä *et al. Geotherm Energy* (2020) 8:17

Page 3 of 21

the core scale. Colombani et al. (2015) validated the solute transport model with heat transport in a sandy aquifer. Kocabas (2005) and Ma et al. (2012) compared solute and heat transport in evaluating the hydraulic properties of the subsurface.

In this study, we estimate fluid flow characteristics (solute tracer recovery, mean residence time, swept volume, and mean fluid velocity) of a fractured and stimulated crystalline rock mass at ambient temperatures (about 13 °C) and approximately 2 weeks after the start of hot water (about 45 °C) injection. These estimated characteristics are derived from two dye tracer tests, conducted before and during the hot water injection. Our experiments were conducted at the Grimsel Test Site (GTS) in Switzerland, which is operated by the Swiss National Cooperative for the Disposal of Radioactive Waste (Nagra). By comparing those results before and during hot water injection, we investigate the effects of the hot water injection on the fluid flow characteristics of the fracture-dominated rock mass. Moreover, at the same locations, where solute tracer breakthrough curves were recorded, temperature measurements were collected throughout the hot water injection period. Using these temperature measurements, we estimate the fracture surface area that may have contributed to the heat exchange between the host rock and the circulating fluid in the fractures. These estimates, based on a simple parallel plate model, facilitate delineating the fracture geometry at the test site. Our results can be useful for establishing a three-dimensional discrete fracture network (DFN) model of the study site. With the decameter-scale field tracer experiments presented here, we can quantitatively address the knowledge gap regarding inter-well changes in fluid flow properties that are associated with hot water injection into a fracture-dominated crystalline rock.

Test site

The Grimsel Test Site (GTS) is located in the Swiss Alps at 1733 m a.s.l. with 400–500 m of overburden, at the boundary between the crystalline rocks of the Central Aare Granite and the Grimsel Granodiorite (Keusen et al. 1989). Between years 2015 and 2017, the GTS hosted the in situ Stimulation and Circulation (ISC) experiment, which aimed at studying the thermo-hydro-mechanical and seismic (THMS) processes relevant for permeability enhancement during high-pressure fluid injections at the decameter scale, and to evaluate the creation of a sustainable heat exchanger (Amann et al. 2018; Krietsch et al. 2018; Gischig et al. 2019). Although the GTS is cold (the ambient rock temperature is 13 °C) and shallow (approximately 500 m deep), in comparison to actual EGS conditions, the test site enables detailed characterizations of the rock mass and comprehensive observations of the permeability enhancements to be made during actual EGS developments. The rock mass permeability was shown to be enhanced, at least temporarily, after the hydraulic stimulation experiments (first hydraulic shearing and then hydraulic fracturing). In addition, new hydraulic connections, enabling larger tracer-swept volumes, were observed (Kittilä et al. 2020), employing both solute tracers and DNA-Labeled Silica Nanotracers (Mikutis et al. 2018; Kong et al. 2018; Kittilä et al. 2019).

At the GTS, two distinguishable shear zones are recognized, intersecting the granodioritic host rock: (i) the ductile NEN–SWS striking S1 and (ii) the younger brittle–ductile E–W striking S3 shear zone (Fig. 1) (Keusen et al. 1989). There exists also a ductile shear zone, classified as S2, which is slightly discordant to S1; however,

Kittilä *et al. Geotherm Energy*   (2020) 8:17

Page 4 of 21

Fig. 1 Overview of the experiment setup at the Grimsel Test Site (GTS) (modified from Krietsch et al. 2018). The shear zone structures, designated S1 and S3, are shown as red and green planes, respectively. There is also a shear zone classified as S2, which is slightly discordant to S1. However, the S1 and S2 shear zones cannot be distinguished in the field (Keusen et al. 1989; Krietsch et al. 2018). The injection and monitoring intervals, associated with this study, in boreholes INJ1, INJ2, PRP1, and PRP2 (black cylinders) and the AU Tunnel outflow point (black circle) are marked. The orange arrows indicate the interpreted flow directions in injection interval INJ2-int4, where the arrows with solid lines are associated with the more prominent flow directions (see Section 'Redistribution of fluid flow' for more information)

the S1 and S2 shear zones cannot be distinguished in the field (Keusen et al. 1989; Krietsch et al. 2018). The dominant S3 shear zone is composed of two structures that are associated with biotite-rich metabasic dykes that are up to 1 m thick and approximately 2.5 m apart (Krietsch et al. 2019). The two S3 shear zone structures, varying in thickness from 38 to 312 mm (Krietsch et al. 2018), bound a highly fractured zone, where the fracture density is about $20\,\text{m}^{-1}$ (Jalali et al. 2017; Krietsch et al. 2018). Most of the open fractures, identified in the INJ1 and INJ2 boreholes (Fig. 1), employing optical televiewer (OPTV) logs, are associated with this highly fractured zone (Jalali et al. 2018b; Krietsch et al. 2018). There are also some partially open fractures (Jalali et al. 2018b; Krietsch et al. 2018), containing cataclasites, breccias, and fault gouge (Ziegler et al. 2013). The highly fractured zone is seen in seismic tomograms as a low-velocity zone (Krietsch et al. 2018) and in tracer tomograms as a zone of high hydraulic conductivity (Kittilä et al. 2020). The host rock beyond the shear zone structures is remarkably intact, with 0–3 fractures per meter (Gischig et al. 2018).

Fluid flow at the ISC test site is dominated by the highly fractured zone and the drainage effect of the AU Tunnel (Jalali et al. 2017; Krietsch et al. 2018; Kittilä et al. 2020), with an average natural discharge of $100\,\text{ml}\,\text{min}^{-1}$ at the AU Tunnel (Jalali et al. 2018b). The transmissivity of the shear zones ranges from 10^{-12} to $10^{-6}\,\text{m}^2\,\text{s}^{-1}$ (Brixel et al. 2020a, b), and in the intact rock, the average transmissivity is less than $10^{-13}\,\text{m}^2\,\text{s}^{-1}$ (Keusen et al. 1989; Jalali et al. 2018a).
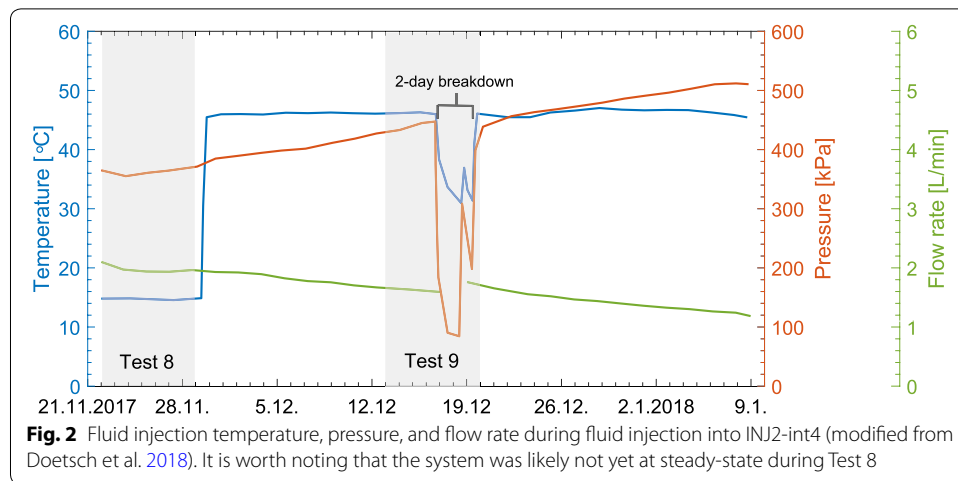
Fig. 2 Fluid injection temperature, pressure, and flow rate during fluid injection into INJ2-int4 (modified from Doetsch et al. 2018). It is worth noting that the system was likely not yet at steady-state during Test 8

Table 1 Summary of tracer injection and production during Tests 8 and 9

Metric	Test 8	Test 9
Test start	22.11.2017	13.12.2017
Hot water injection	29.11.2017–10.01.2018	
Test end	29.12.2017	20.12.2017
Injection interval	INJ2-int4	
Injection depth (m)	22.89–23.89	
Injection flow rate, Q_{inj} (L min^{-1})	2.1	1.8
Injection pressure, P_{inj} (kPa)	374	450
Injection temperature, T_J (°C)	13	45
Tracer	Eosine	
Injected tracer mass, M_{inj} (mg)	19.5	19.0
Injected tracer volume, V_{inj} (L)	0.975	0.950
Monitoring locations	AU Tunnel, PRP1-int3	
	PRP2-int2, PRP1-int2	
Production flow rate, Q_{pro} (L min^{-1})	1[a], 0.090	0.85[a], 0.051
	0.069, 0.12	0.043, 0.12
Distance to monitoring location (m)	20.7, 4.6, 6.4, 8.6	

[a] The production flow rate at the AU Tunnel is estimated for both Test 8 and Test 9, as no measurements are available. Details are given in 'Results and discussion' section

Methods

Tracer experiments

Two solute dye tracer tests were conducted during the 'Circulation' phase of the ISC experiment (no actual fluid reinjection took place). The objective was to study the effects of hot water injection on fluid flow in the stimulated fractured rock mass. The first test, namely Test 8, was conducted immediately before the start of the hot water injection. The second test, namely Test 9, was conducted during the hot (45 °C) water injection, which, at that time, had been continued for 2 weeks. In both tests, the solute dye tracers were injected into the fractured rock as a short pulse. Table 1 summarizes the details of tracer injection and production during Tests 8 and 9, and Fig. 2 shows the injection temperature, pressure, and flow rate during the hot water

injection experiment. The tracers and the hot water were injected into Interval 4 in Borehole INJ2 (hereafter INJ2-int4), while tracer concentrations and water temperature were monitored at borehole intervals INJ1-int4, PRP1-int3, PRP2-int2, and PRP1-int2 as well as at the AU Tunnel outflow point (Fig. 1 and Table 1). However, at INJ1-int4 the production flow rate was approximately $1\,\mathrm{ml\,min^{-1}}$ during Test 8 and during Test 9, the outflow at that location had already ceased. Hence, no tracer data were recovered from INJ1-int4.

Injection of tap water was continued throughout the 'Circulation' phase, with a mean flow rate of $2.1\,\mathrm{L\,min^{-1}}$ during Test 8 and $1.8\,\mathrm{L\,min^{-1}}$ during Test 9. While the injection flow rate decreased, the injection pressure (absolute pressure at the wellhead) increased from about 374 kPa during Test 8 to about 450 kPa during Test 9 (Table 1 and Fig. 2). However, as Fig. 2 shows, it is important to note, based on the changes in the injection pressure and flow rate, that the system was likely not yet at steady-state during Test 8. At the monitoring locations, tracer signals were continuously monitored using flow-through fluorometers (GGUN-FL30). The signals (in millivolts) from these fluorometers were converted to tracer concentrations using laboratory-analyzed discrete samples (Luminescence Spectrometer, Perkin Elmer, LS 50 B), collected at the monitoring locations (Table 1).

Moment analysis

In this study, the effect of hot water injection on fluid flow redistribution in the fractured crystalline rock at the GTS is characterized using tracer-determined residence time distribution (RTD) curves. It is well known that RTD curves can be described statistically by determining the mode (tracer recovery), integral mean (tracer mean residence time), and width (dispersion) of the distribution (Robinson and Tester 1984; Leube et al. 2012). Further interpretation of the RTD curve moments allows the calculation of the volume swept by the tracer, the flow geometry, and the Gini coefficient, which expresses the flow heterogeneity in the fracture system (Shook and Forsmann 2005; Shook and Suzuki 2017).

The concept of RTD curves was developed by Danckwerts (1953), where the distribution of tracer residence times, $E(t)$, depends on the fraction of the tracer that has a residence time between time t and $t + \mathrm{d}t$ in the system. This fraction is given by $E(t)\mathrm{d}t$. Thus, for the tracer concentration, $c(t)$, at time t of the effluents at a monitoring location, the RTD curve is calculated as

$$E(t) = \frac{c(t)\rho q_{\mathrm{pro}}}{M_{\mathrm{inj}}},\tag{1}$$

where ρ is the effluent density, q_{pro} the volumetric production flow rate at the monitoring location, and M_{inj} the mass of injected tracer at the injection location (Robinson and Tester 1984; Shook and Forsmann 2005). The nth temporal moment of an RTD curve is then defined as

$$m_n^* = \int\limits_0^\infty t^n E(\mathbf{x},\, t)\,\mathrm{d}t.\tag{2}$$

The zeroth temporal moment yields the tracer recovery, $R = m_0^*$. The first normalized temporal moment defines the mean residence time,

$$t^* = \frac{m_1^*}{m_0^*}, \tag{3}$$

and the second centralized and normalized temporal moment provides the measure on tracer dispersion,

$$m_{2,c} = \frac{m_2^*}{m_0^*} - \left(\frac{m_1^*}{m_0^*}\right)^2. \tag{4}$$

For tracer tests, where tracers are injected as a pulse, the tracer-swept volume is defined as Shook and Suzuki (2017)

$$V_p = Rt^* q_{inj}, \tag{5}$$

where q_{inj} is the volumetric injection flow rate. The flow geometry in a fractured medium can be characterized by the flow capacity–storage capacity curve ($F - \Phi$ curve). The $F - \Phi$ curve is a cumulative contribution of individual flow paths, where the flow capacity, F, is the specific velocity, divided by the bulk velocity, and the storage capacity, Φ, is the fraction of the pore volume associated with that flow path (Shook and Forsmann 2005; Shook and Suzuki 2017). In specific, the $F - \Phi$ curve is mathematically expressed as

$$F(t) = \frac{\int\limits_0^t E(\tau)d\tau}{\int\limits_0^\infty E(t)\mathrm{d}t} \tag{6}$$

and

$$\Phi(t) = \frac{\int\limits_0^t E(\tau)\tau d\tau}{\int\limits_0^\infty E(t)t\mathrm{d}t}. \tag{7}$$

A homogeneous system yields a diagonal line in the $F - \Phi$ plot, where F and Φ range between 0 and 1. For a heterogeneous system, on the other hand, abrupt breaks in the $F - \Phi$ curve's slope give insights into the presence of different permeabilities (Shook 2003; Shook and Suzuki 2017). Furthermore, the heterogeneity of a system can be quantified from the $F - \Phi$ curve by determining the Gini coefficient,

$$G = 2\left\{\int\limits_0^1 F\, d\Phi - \frac{1}{2}\right\}. \tag{8}$$

The G value varies between 0 and 1, where a homogeneous system yields 0, and 1 means that a negligibly small fraction of the total tracer-swept volume provides almost all of the fluid (Shook and Forsmann 2005).

Kittilä *et al. Geotherm Energy*   (2020) 8:17

Page 8 of 21

Temperature perturbations in a fracture

To estimate the fracture surface area between the injection and monitoring locations, we apply an analytic solution, given by Shook and Suzuki (2017), for a single fracture with uniform aperture. This analytic solution utilizes the tracer-swept volume from the conservative tracer tests and fluid temperature measurements to approximate the temperature distribution in a single fracture. Following the governing equations in Gringarten and Sauty (1975), which are similar to those published by Lauwerier (1955) and Carlslaw and Jaeger (1959), the heat transport in a half of a single fracture, with heat flow across the rock matrix–fracture interface, is given by

$$\frac{b}{2}(\rho C_p)_F \frac{\partial T_W}{\partial t} + \frac{q_{\text{pro}}}{2}(\rho C_p)_W \frac{\partial T_W}{\partial S} - K_R \frac{\partial T_R}{\partial z}\mid_{z=b/2} = 0, \tag{9}$$

where b is the fracture aperture, C_p is heat capacity, and T is temperature, with subscripts F for fracture, W for water, and R for rock matrix. S is the surface area of the half fracture, K_R is the thermal conductivity of the rock matrix, and $(\rho C_p)_F = \phi(\rho C_p)_W + (1 - \phi)(\rho C_p)_R$. In the current setup, the half fracture is bounded by the center of the fracture at $z = 0$ and the rock matrix–fracture interface at $z = b/2$. The temperature evolution of the surrounding rock matrix is governed by the heat conduction equation

$$\frac{\partial^2 T_R}{\partial z^2} = \frac{(\rho C_p)_R}{K_R}\frac{\partial T_R}{\partial t} \quad \text{for } z \geq \frac{b}{2}. \tag{10}$$

The temperatures must also satisfy the following boundary and initial conditions:

$$T_W(S,t) = T_R(S,z,t) = T_I \qquad \text{for } t \leq \frac{\phi b S}{q_{\text{pro}}}, \tag{11}$$

$$T_W(0,t) = T_J \qquad \text{for } t > 0, \tag{12}$$

$$T_W(S,t) = T_R(S,b/2,t) \qquad \forall S,t, \tag{13}$$

$$\lim_{z \to \infty} T_R(S,z,t) = T_I \qquad \forall S,z,t, \tag{14}$$

where T_I and T_J are the initial and the injection temperature, respectively. The analytical solution of Eqs. (9) and (10), subject to the conditions given by Eqs. (11)–(14), is given by Gringarten and Sauty (1975) as

$$\frac{T_I - T_W(t)}{T_I - T_J} = \text{erfc}\left[\frac{(\rho C_p)_W^2}{K_R(\rho C_p)_R}\left(\frac{q_{\text{pro}}}{S}\right)^2\left\{t - \frac{(\rho C_p)_T}{(\rho C_p)_W}\frac{bS}{q_{\text{pro}}}\right\}\right]^{-1/2}. \tag{15}$$

By taking the tracer-swept volume, $V_p = bWL\phi = bS\phi$, and the total fracture surface area, $A = 2S$, where W and L are the fracture width and length, respectively, and multiplying the last term in Eq. (15) by ϕ/ϕ and simplifying, Shook and Suzuki (2017) obtained

Kittilä *et al. Geotherm Energy* (2020) 8:17

Page 9 of 21

$$T_W(L,t) = T_I - (T_I - T_J)\text{erfc}\left[\frac{1}{(\rho C_p)_W}\frac{A}{2q_{\text{pro}}}\sqrt{\frac{K_R(\rho C_p)_R}{t - \frac{(\rho C_p)_F}{(\rho C_p)_W}\frac{V_p}{\phi q_{\text{pro}}}}}\right].\tag{16}$$
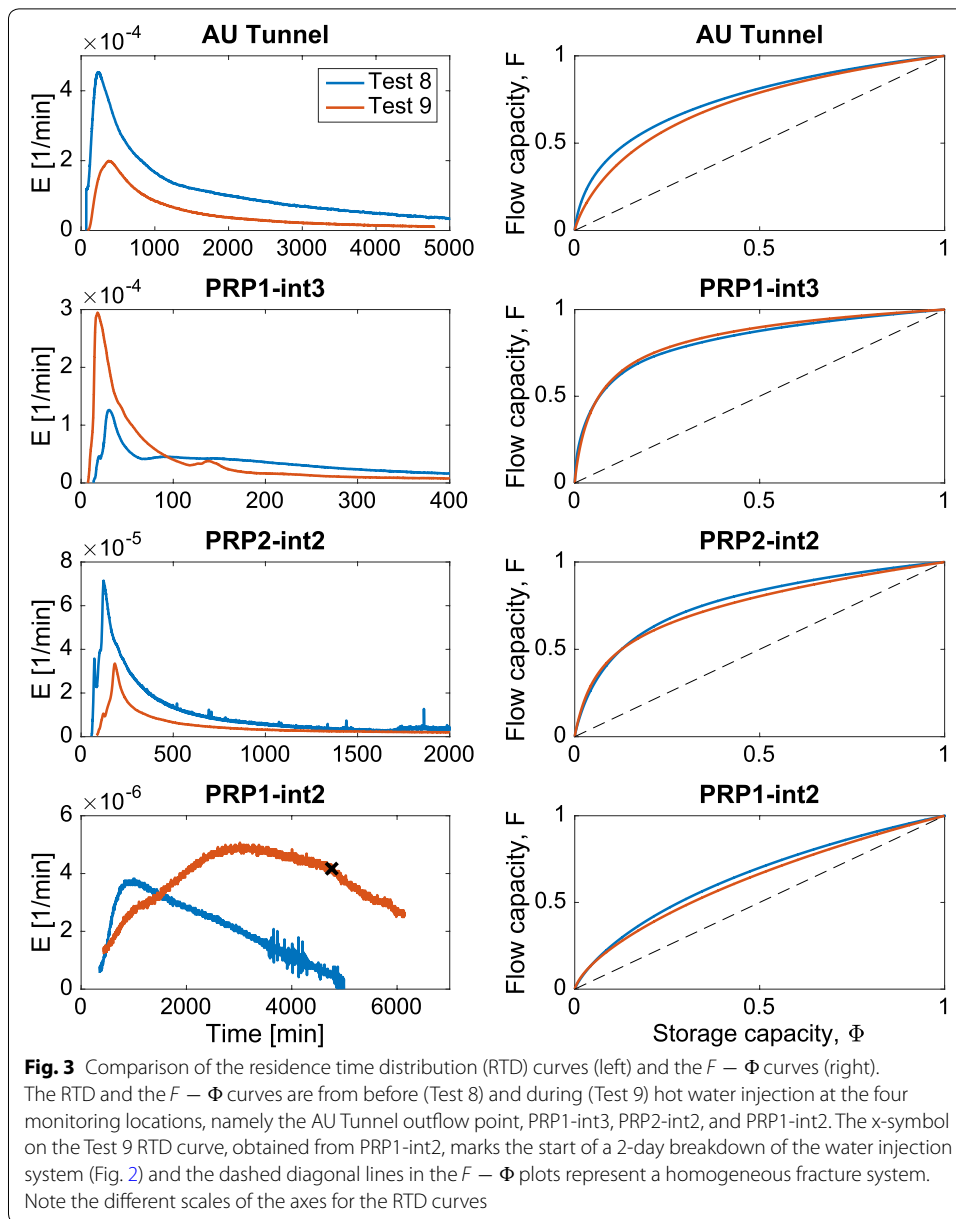
Equation (16) can be used to estimate the surface area of a fracture, A, through which heat exchange between the fluid and the rock takes place. Here, A is constrained by the measurable V_p from the solute tracer tests and by temperature observations in the monitoring borehole. The variables T, q_{pro}, K_R, and C_p can be obtained from measurements or from literature data, while porosity, ϕ, can be estimated, as its influence on the results is minor (Shook and Suzuki 2017).

Results and discussion

Residence time distributions

Figure 3 shows the residence time distributions (RTDs) and the $F - \Phi$ curves from the four monitoring locations, obtained during Tests 8 and 9. The minor changes in the $F - \Phi$ curves between Tests 8 and 9 suggest that the injected heat had a minor influence on the distribution of fluid within the tracer-swept volumes. The $F - \Phi$ curves from PRP1-int2 display exceptionally negligible deviations from the $F - \Phi$ diagonal line, implying a rather homogeneous flow distribution. In contrast, the largest deviations of the $F - \Phi$ curves from the diagonal line are observed at PRP1-int3, where approximately 81% of the recovered tracer is transported through only 30% of the total tracer-swept volume. In another tracer test at the same test site and at the same observation interval (i.e., PRP1-int3) but injecting a tracer at a different interval, namely INJ1-int4 instead of INJ2-int4 (as reported in this study, Fig. 1), Kittilä et al. (2019) reported that 30% of the tracer-swept volume contributed to 70% of the tracer recovered from PRP1-int3. Robinson and Tester (1984) observed that the flow impedance of local fracture outlets can mask dispersive changes within a system by dominating the distribution of fluid flow. Therefore, the observed similarity in the distribution of flow at PRP1-int3 from two opposite injection locations suggests that most of the flow distribution may occur near the fracture outlet at PRP1-int3.

Contrary to the similarity of the $F - \Phi$ curves, the RTD curves show distinct differences between Tests 8 and 9 (Fig. 3). During Test 9, the tracer was less likely arriving at the AU Tunnel and PRP2-int2 than before the hot water injection, as indicated by the overall lower age distribution, i.e., E values between the tests, recorded at these two monitoring locations (Fig. 3). Furthermore, the RTD curves from the AU Tunnel and PRP2-int2 are highly similar in shape during both tracer tests. However, tracer arriving at PRP1-int3 was more likely transported in the main preferential flow paths than before the hot water injection, resulting in higher peak E values in the RTD curve. In contrast, the long tailing observed during Test 8 is not as prominent in the RTD curve from Test 9 at PRP1-int3, as the peak E value more than doubled (Fig. 3). At PRP1-int2, the E values were also higher during Test 9 but accompanied by later tracer arrival times than during Test 8. Also, the peak arrival time (given in Table 2) increased by more than 200%. Unfortunately, we were not able to obtain a sufficient record of the tailing before the test was terminated. The x-symbol in the RTD curve, obtained from PRP1-int2 during Test 9 (Fig. 3), marks the start of a 2-day breakdown of the water injection system, i.e.,

Fig. 3 Comparison of the residence time distribution (RTD) curves (left) and the $F - \Phi$ curves (right). The RTD and the $F - \Phi$ curves are from before (Test 8) and during (Test 9) hot water injection at the four monitoring locations, namely the AU Tunnel outflow point, PRP1-int3, PRP2-int2, and PRP1-int2. The x-symbol on the Test 9 RTD curve, obtained from PRP1-int2, marks the start of a 2-day breakdown of the water injection system (Fig. 2) and the dashed diagonal lines in the $F - \Phi$ plots represent a homogeneous fracture system. Note the different scales of the axes for the RTD curves

approximately 4800 min, or about 80 h, after the pulse injection of the solute dye tracer (Fig. 2), which likely had an effect on the tailing of the PRP1-int2 RTD curve by changing its decay rate.

Redistribution of fluid flow

Changes in flow rate and tracer recovery

Table 2 shows the tracer transport results from the moment analysis. These results are calculated from the obtained RTD curves without extrapolation. The recovery, R, becomes smaller at all of the monitoring locations during Test 9, except at PRP1-int2, indicating that the injection of ~ 45 °C hot water redistributed the fluid flow in the

Table 2 Summary of the tracer transport parameters

Monitoring location	Test 8	Test 9	Change[a] (%)
Recovery, R (%)			
AU tunnel	$\sim$ 65	$\sim$ 23	− 64
PRP1-int3	2.84	2.02	− 29
PRP2-int2	2.47	1.46	− 41
PRP1-int2	0.97	2.17	123
Peak arrival time, t_p (min)			
AU tunnel	235	375	60
PRP1-int3	30	18	− 41
PRP2-int2	122	183	50
PRP1-int2	950	3020	218
Mean residence time, t^* (min)			
AU tunnel	2242	1383	− 38
PRP1-int3	1232	286	− 77
PRP2-int2	866	1511	75
PRP1-int2	2126	3373	59
Swept volume, V_p m³			
AU tunnel	$\sim$3.05	$\sim$0.57	− 81
PRP1-int3	0.074	0.010	− 86
PRP2-int2	0.045	0.040	− 12
PRP1-int2	0.043	0.13	202
Dispersion, $m_{2,c}$ (min²)			
AU tunnel	4.63E+06	1.31E+06	− 72
PRP1-int3	2.76E+06	1.91E+05	− 93
PRP2-int2	8.54E+05	1.94E+06	127
PRP1-int2	1.24E+06	2.15E+06	73
Gini coefficient, G (−)			
AU tunnel	0.50	0.44	− 13
PRP1-int3	0.64	0.67	4
PRP2-int2	0.54	0.50	− 7
PRP1-int2	0.30	0.25	− 16

[a] Change from Test 8 to Test 9

fracture network of the S3 shear zone structures, resulting in a substantial overall reduction of total tracer recovery (Table 2).

It is worth noting that the tracer recoveries at the AU Tunnel are calculated with an estimated production flow rate, due to an overflow at the outflow collection point, using a "tipping-bucket" measuring device. In our previous tracer tests, at the GTS (Kittilä et al. 2020), an outflow of about 1.0 L min^{-1} was documented at the AU Tunnel. Therefore, we estimate a production flow rate of 1.0 L min^{-1} during Test 8, and yield a tracer recovery of 65% at the AU Tunnel (Table 2). This calculated recovery is a typical value, observed during previous tracer tests at the GTS (Kittilä et al. 2020). Consequently, we also use 1.0 L min^{-1} in estimating the tracer-swept volume (Eq. 5 and Table 2).

During Test 9, we have noticed that the overflow at the AU Tunnel outflow collection point was not as significant as it had been during Test 8. This reduction of production flow rate at the AU Tunnel during Test 9 is physically rational because a good hydraulic connection between the injection interval INJ2-int4 and the AU Tunnel has

been observed during previous tests at the GTS (Jalali et al. 2018b; Brixel et al. 2020a; Kittilä et al. (2020). Here, we propose two methods to estimate the production flow rate at the AU Tunnel during Test 9. Method I uses a direct proportion of the injection rate, i.e., $Q^{AU}_{\text{pro,Test9}} = Q^{AU}_{\text{pro,Test8}} \times Q_{\text{inj,Test 9}}/Q_{\text{inj,Test 8}}$. As previously discussed, we estimate that $Q_{\text{pro,Test 8}} = 1.0\,\text{L min}^{-1}$. Given that $Q_{\text{inj,Test 8}} = 2.1\,\text{L min}^{-1}$ and $Q_{\text{inj,Test 9}} = 1.8\,\text{L min}^{-1}$ (Table 1), $Q^{AU}_{\text{pro,Test 9}}$ is calculated to be $0.85\,\text{L min}^{-1}$. Method II uses the proportional fluid lost to the far-field. In this method, the fraction of fluid lost to the far-field is defined in terms of injection vs. production flow rate, i.e., not referring to recovered tracer mass. We assume that the fraction of fluid lost to the far-field is the same during Tests 8 and 9. During Test 8, the fraction of fluid lost to the far-field is calculated as $f_{\text{lost}} = 1 - \sum_i Q^i_{\text{pro,Test 8}}/Q_{\text{inj,Test 8}}$, where the summation applies to all monitoring locations (i.e., i represents the AU Tunnel, PRP1-int3, PRP2-int2, and PRP1-int2). Taking the injection and the production flow rates in Table 1, f_{lost} is calculated to be 0.39. According to the assumption made for Method II, $Q^{AU}_{\text{pro,Test9}} = Q_{\text{inj,Test 9}} \times (1 - f_{\text{lost}}) - \sum_j Q^j_{\text{pro,Test 8}}$, where j represents the monitoring locations, excluding the AU Tunnel. Method II yields $Q^{AU}_{\text{pro,Test 9}} = 0.88\,\text{L min}^{-1}$. Both Methods (I and II) yield very similar production flow rates at the AU Tunnel during Test 9. The production flow rate of $0.85\,\text{L min}^{-1}$ yields a tracer recovery of 23% and a swept volume of $0.57\,\text{m}^3$ at the AU Tunnel (Table 2). Even if taking the same production flow rate (i.e., $1.0\,\text{L min}^{-1}$) as estimated during Test 8, we obtain a tracer recovery of 27% and a swept volume of $0.68\,\text{m}^3$ at the AU Tunnel. It is thus evident that the decrease in tracer recovery is significant between Tests 8 and 9, implying that the hot water injection greatly impaired the hydraulic connection from INJ2-int4 to the AU Tunnel. Furthermore, these results suggest that a significant portion of the injected tracer was lost to the far-field.

The injection of hot water promotes the closure of fractures (National Research Council 1996). Such closures occur particularly in fractures that initially carried higher fluid flow rates, thereby closing sooner. This fracture closure upon hot fluid injection into rock fractures is caused by the thermal expansion of the fluid-heated rock matrix (Rutqvist et al. 2001). The closure of the fractures in turn causes the fluid to flow through new pathways. The opposite effect, that is the focusing of fluid flow in cooled zones, resulting from thermal contraction of the rock matrix when cold fluids are injected into a rock fracture, was observed by Fu et al. (2016). Consequently, hydraulic connections between injection and monitoring locations can become weakened either (i) by hot fluid injection, when key flow paths are constricted, or (ii) by cold fluid injection, when certain flow paths begin receiving more fluid, diminishing fluid flow through other flow paths and compromising previously dominant hydraulic connections.

Visual inspections of the S3 shear zone structures show that the injection interval INJ2-int4 is located in-between the S3.1 and S3.2 shear zones (Fig. 1 and the schematic illustration of the same study site in Brixel et al. (2020a)). It is also observed that the AU Tunnel outflow point is located in-between these two structures (Krietsch et al. 2018). It is thus likely that the solute tracer injected in the current study during Test 8 first travelled via a linking damage zone, i.e., fractures linking S3.1 and S3.2, to a wall damage zone, i.e., fractures parallel to and associated with S3.1 and/or S3.2 (Brixel et al. 2020a, b). The flow directions mentioned here are shown as orange arrows in Fig. 1. We

can speculate that, subsequently, the tracers entered the highly fractured zone between S3.1 and S3.2 again, and then exited at the AU Tunnel outflow point (Fig. 1). This interpretation is further supported by the Time-Lapse Difference Reflection Ground Penetrating Radar (GPR) surveys conducted at the GTS (Giertzuch et al. 2019). However, from INJ2-int4 toward the west, i.e., toward the other monitoring locations at the right side of Fig. 1, the solute tracer travelled faster through the S3.1 shear zone (RTDs from PRP1-int3 and PRP2-int2) than through the S3.2 shear zone (RTD from PRP1-int2).

During Test 9, the injection flow rate, Q_{inj}, was lower than during Test 8, whereas the injection pressure, P_{inj}, had increased (Table 1). Note that the injection pressures during Tests 8 and 9 never exceeded the minimum stress at the site, nor the pore pressure required to initiate rock failure (8.6–9.7 MPa for σ_3 and 5 MPa, respectively Krietsch et al. (2019)). Therefore, the fracture system was not supported by the injection pressure. In addition to the changes in the injection flow rate and fluid pressure, the production flow rates, Q_{pro}, at PRP1-int3, PRP2-int2, and PRP1-int2 (Table 1) were 43%, and 38% less, and 2% more, respectively, than during Test 8. Such changes in the injection and production flow rates and fluid injection pressures were also observed in a hot water thermal tracer test in another fracture zone, located only 300 m north from our test volume, at the GTS (Marschall et al. 1995).

In terms of negative or positive changes, regarding production flow rates and tracer recoveries during Test 8 and Test 9, the two parameters behave similarly (Table 2). In terms of quantity, however, the changes between these two parameters do not match. This may be due to different contributions of fluid flow from the far-field into the monitoring locations, due to the redistribution of flow (and changes in the fluid pressure gradient) in the fracture network.

Tracer-swept volumes and residence times

Similar to tracer recoveries, the tracer-swept volumes, V_p, decreased at all monitoring locations, except at PRP1-int2 (Table 2). Although the full RTD curve could not be recorded at PRP1-int2 during Test 9, this interval indicated a strong increase in tracer-swept volume from 0.043 m^3 to 0.13 m^3. The decrease in tracer-swept volume at the other three monitoring locations likely reflects the diminished quantities of the traced water traveling to the monitoring locations. It is important to note that the tracer-swept volume yields an estimate of the total volume of all fractures that contribute to fluid flow and that produce fluid at a monitoring location, regardless of the fractures' flow impedances. Typically, the majority of the injected fluid flows in low-impedance fractures, yielding an $F - \Phi$ curve with a deviation from the $F - \Phi$ diagonal line. However, extremely long fluid residence times usually indicate that low permeabilities and/or long-distance flow paths are present.

As discussed earlier, thermally driven fracture closure can significantly affect the distribution of fluid flow, as it diminishes fluid flow in the heated zones. The mean residence times, t^*, were shorter during Test 9 at the AU Tunnel and PRP1-int3, and longer at PRP2-int2 and PRP1-int2, than during Test 8. Furthermore, the change in the mean residence time appears to be directly proportional to the change in dispersion, $m_{2,c}$, during the tracer tests (Table 2). The dispersion values describe the spread of tracer residence times. If $m_{2,c}$ yielded zero, tracer introduced to the system by a Dirac pulse, and

observed at a monitoring location, would have experienced zero dilution. However, natural systems invariably yield nonzero $m_{2,c}$, as the tracer is always transported with at least some variation in the fluid flow velocity field in the systems (Cirpka and Kitanidis 2000). These results suggest that, at the AU Tunnel and at PRP1-int3, not only was the bulk of the tracer transported faster during Test 9, but also the occurrence of the tracer mass recovered from the flow paths with long residence times decreased. Consequently, the opposite describes the RTD curves obtained from PRP2-int2 and PRP1-int2. That is, the slower traveling tracers were more likely diffusing into stagnant zones.

Gini coefficients

The Gini coefficient, *G*, indicates how channelized the fluid flow is. Only the RTD curve, obtained from PRP1-int3, yielded an increased Gini coefficient after the start of hot water injection. This likely reflects the domination of the preferential flow paths over the total tracer transport toward PRP1-int3 during Test 9, which is exhibited as a higher peak of *E* values in the RTD curve (Fig. 3). In contrast, the changes in values of dispersion indicator ($m_{2,c}$) and Gini coefficients at the AU Tunnel indicate that both the spread of the residence times had decreased and the fluid flow was less channelized during Test 9 than during Test 8. However, despite the decrease, or only small increase, in all of the Gini coefficient values during Test 9, the fracture network, associated with the S3 shear zone, still exhibited a rather heterogeneous distribution of fluid flow (i.e., Gini coefficients ranging from 0.44 to 0.67, excluding the Gini coefficients from PRP1-int2; 0.25-0.30).

Estimation of fracture surface area

The initial fluid temperature at the GTS was approximately 13 °C (Table 3). Combined datasets of solute dye tracer RTD curves and temperature measurements were recorded at the AU Tunnel outflow point, PRP1-int3, PRP2-int2, and PRP1-int2. The temperature data used in this paper, recorded at these monitoring locations, were obtained with PT1000 temperature sensors, installed in the open intervals (Doetsch et al. 2018). At the AU Tunnel outflow point, the temperature measurements were strongly influenced by the direct contact of the outflow, at the tunnel wall, with the atmosphere (Brixel et al. 2019), and are thus not analyzed in this study. During Test 9, the temperature at PRP1-int3 was fluctuating, with a harmonic mean of 20.2 °C. At PRP2-int2, the temperature was still steadily increasing, by approximately 0.05 °C per day, with a harmonic mean during Test 9 of 13.5 °C. At PRP1-int2, no increase in temperature was observed (Table 3 and Fig. 4).

When injecting water that is cooler or hotter than the in situ fracture temperature, the induced temperature perturbations at a monitoring location at time *t* are related to the surface area of the fractures contributing to fluid flow (Kolditz 1995; Finsterle et al. 2013; Guo et al. 2016). Thus, to provide constraints on fracture geometry, Eq. (16) is solved for the three monitoring locations during Test 9 (Table 4), using a fracture porosity of $\phi = 0.80$ (Marschall et al. 1995) (Table 3). However, it is worth noting that only at PRP1-int3 the temperature perturbation signal is significant, in addition to apparently having reached steady-state. As the temperature perturbations in Table 3 and Fig. 4 show, heat takes a long time to break through when the
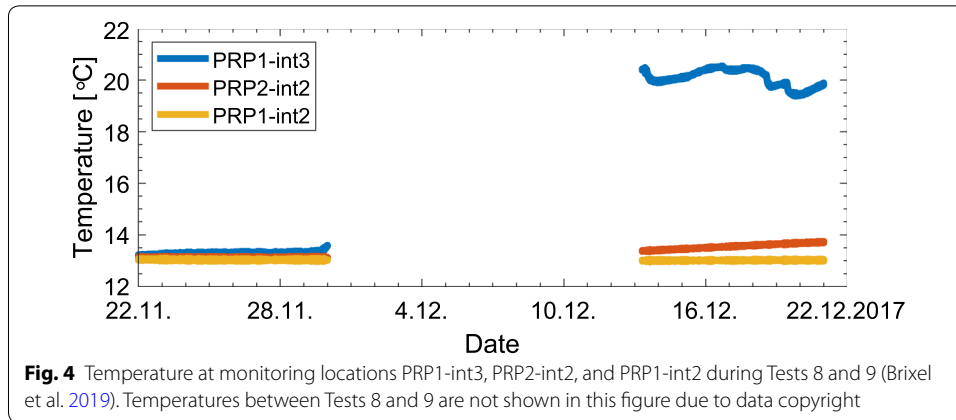
Fig. 4 Temperature at monitoring locations PRP1-int3, PRP2-int2, and PRP1-int2 during Tests 8 and 9 (Brixel et al. 2019). Temperatures between Tests 8 and 9 are not shown in this figure due to data copyright

Table 3 Summary of thermal and petrophysical properties used

Model parameters	
ρ_R	2706[a]
$C_{p,R}$	768[b]
K_R	3.25[b]
ρ_W (13 °C)	999
$C_{p,W}$ (13 °C)	4180
T_I	13[c]
T_J	45[c]
ϕ	0.8
t (days)	15
T_W (AU Tunnel)	N/A[c]
T_W (PRP1-int3)	20.2[c]
T_W (PRP2-int2)	13.5[c]
T_W (PRP1-int2)	13.0[c]

[a] Wenning et al. (2018)

[b] Kant et al. (2017)

[c] Brixel et al. (2019)

Table 4 Results of solving fracture surface area using Eq. (16)

Monitoring	Test 9	
Location	A (m^2)	b (mm)
PRP1-int3	2.65	9.4
PRP2-int2	4.40	22.7
PRP1-int2	> 19.0	< 17.1

scale of a system is increased. For typical reservoir scales of hundreds of meters, such long breakthrough times would often be unfeasible to estimate the fracture surface area from the comparison of heat and conservative tracer breakthrough data. Consequently, thermally degrading or reactive tracers have been suggested to be compared with conservative and non-reactive tracers to estimate fracture surface areas (Hawkins et al. 2017, 2018).

As pointed out by Shook and Suzuki (2017), Eq. (16), i.e., the estimation of the fracture surface area, A, is not particularly sensitive to the estimation of ϕ. In fact, the aperture of a single fracture does not influence the estimate of its surface area. In contrast, for highly fractured reservoirs, the fracture porosity (taken as $2b/L$, where b and L are the fracture aperture and spacing, respectively) strongly influences surface area. However, the breakthrough time of a conservative tracer is strongly influenced by the reservoir volume, i.e., the mean fracture aperture, whereas the heat exchange in fractured reservoirs is dominated by the surface area available for heat exchange (Hawkins et al. 2017a, b). Therefore, there is an uncertainty in estimating thermal breakthrough times and fracture surface areas using conservative tracer tests. In summary, the non-unique relationship between solute and heat transport limits the accuracy of determining fracture surface areas, employing the simple model proposed in this study.

Nonetheless, we set t at 15 days in Eq. 16, i.e., 15 days after the start of hot water injection, to estimate the fracture surface area, A (Table 4), with the temperature values measured at the monitoring locations (Table 3). At PRP1-int3, a surface area of $2.65\,\mathrm{m}^2$ is calculated, which enabled the highest temperature change of $\Delta T \approx 7\,^\circ\mathrm{C}$ to be measured during hot water injection (Fig. 4) Doetsch et al. (2018). At PRP2-int2, where only a slight and not yet stabilized temperature perturbation was observed, the production flow rate was lower than at PRP1-int3, and the tracer-swept volume was four times higher. In comparison to PRP1-int3, PRP2-int2 yielded a larger fracture surface area of $A = 4.40\,\mathrm{m}^2$. As no temperature perturbation was observed at PRP1-int2 during Test 9, the fracture surface area is estimated to be $19.0\,\mathrm{m}^2$ (when $\Delta T = 0\,^\circ\mathrm{C}$) or larger (Table 4).

The fracture aperture, b, values, shown in the last column of Table 4, and calculated using the tracer-swept volumes, are directly scaled by porosity, ϕ, which is estimated in this study. Robinson and Tester (1984) point out that placing the flow, provided by the tracer-swept volume, V_p, within a bulk volume of rock requires assuming a porosity, which is difficult to determine. They explain that with a porosity of 1–10%, fluid flow is localized to a small rock volume, such as that formed by interconnected flow paths between main fractures. In contrast, porosities below 1% imply that a larger fraction of the fluid is sweeping through the rock beyond the main fractures. Furthermore, the aperture, b, values are non-unique and are thus only meant to illustrate the potential magnitude of b. Through a numerical model of fluid flow through a nearby fracture system at the GTS, Marschall et al. (1995) found that the best fit for solute breakthrough curves was obtained when fracture apertures were estimated to be approximately 10–80 mm. Thus, our results for b are on the same order of magnitude with the results obtained by Marschall et al. (1995).

Robinson and Tester (1984), Luhmann et al. (2015), and de La Bernardie et al. (2018) point out that heat transfer in fractured media cannot be modeled precisely with a single structure, having constant hydraulic and transport properties. As our results are based on a highly simplified model, they should only serve as scoping calculations. As Fu et al. (2016) and Guo et al. (2016) showed, complex structures can cause thermal perturbations in a rock and a monitoring borehole that deviate from simple models, for example due to flow channeling or as a result of thermally induced fracture aperture variations (Pandey et al. 2017). As the examination of the RTD curves suggests (Fig. 3 and Table 2), it is reasonable to assume that both processes (flow channeling and thermo-mechanical

effects) likely played a role during the hot water injection experiment at the GTS. Despite these complications when estimating heat transfer, employing simple models of solute tracer and temperature data, our results show that this approach still helps placing constraints on fracture geometry. This in turn can improve predictions of the geothermal energy transport performance of a formation.

We believe that the main cause contributing to the redistribution of fluid flow, observed in this study, is most likely the thermo-mechanical expansion of the rock and not, for example, the result of geochemical dissolution of asperities (Grimm Lima et al. 2019), as chemical processes typically involve longer timescales Yasuhara et al. (2011). However, it is important to note that the significance of the system not yet being at steady-state during Test 8, regarding the changes in the moment analysis parameters and the redistribution of fluid flow, cannot be sufficiently determined. In this study, the monitoring location that exhibited the most thermal change (PRP1-int3) is also the location that yielded the highest Gini coefficient and thus represents a hydraulic connection with a highly heterogeneous distribution of fluid flow. In contrast, the monitoring location that exhibited no temperature change (PRP1-int2) is also the location that yielded the lowest Gini coefficient and thus represents a hydraulic connection with a rather homogeneous distribution of fluid flow. With the available data, it is uncertain whether this is a coincidence. However, after the injection of hot water, a heterogeneous distribution of fluid flow apparently tends to focus thermal effects on preferential flow paths, whereas a homogeneous distribution of fluid flow tends to result in the system responding as a whole.

Data uncertainties

In addition to uncertainties regarding the simplification of the thermal perturbation model, it is worth noting that there are other potential sources of uncertainty, including

- Sorption processes and decay of the tracer eosine may have affected the recovered RTD curves. Irreversible sorption would reduce the recovered tracer mass, while reversible sorption would increase the fraction of tracer mass exhibiting long residence times, resulting in long tailing.
- The Test 9 fluorometer data were converted to concentrations (ppb) using the calibration curves from Test 8 and, although there were only two weeks between these tests, it remains unknown how well the calibration curve from Test 8 matches the concentrations during Test 9.
- It is possible that during Test 9, the flow field in the rock volume was still changing, due to the thermal perturbations, i.e., the system was not at steady-state. Consequently, the constant production flow rates, used in Eq. (16) (a mean of the flow rates of Tests 8 and 9), may not have been properly estimated. Also, other fractures than the one(s) producing the injected tracer may have contributed to the total production flow rates. Furthermore, since the start of the hot water injection, the tracer-swept volumes changed. Using the value obtained during Test 9 may thus have underestimated the fracture surface area through which the fluid and rock exchanged heat.
- It may be possible that PRP2-int2 acts as a short-circuiting pathway between the S3.1 and the S3.2 shear zone structures (Fig. 1), because it is intersected by fractures asso-

ciated with both of these structures (Krietsch et al. 2018; Brixel et al. 2020a). The use of tracers in subsurface reservoirs requires installing boreholes, which are likely to change the hydraulic conditions in the subsurface.

Conclusions

We investigated the effects of hot water injection on the hydrodynamic properties of a hydraulically stimulated crystalline rock, using solute dye tracers. The hydraulic stimulations and the tracer tests were part of scaled Enhanced Geothermal System (EGS) analog experiments, which were conducted to gain insights into the processes underpinning permeability enhancement and creation of an efficient subsurface heat exchanger, relevant for the development of actual EGS reservoirs. In addition to comparing the temporal moments and the associated tracer-swept volumes and flow geometries, we put constraints on fracture geometries by estimating the fracture surface areas contributing to heat exchange between the host rock and the fluid flowing in the fractures. Importantly, we observe redistribution of fluid flow and loss of injected fluid to the far-field after 2 weeks of hot water injection, while the key flow paths between the injection and monitoring locations did not change. The obtained results can be interpreted as a manifestation of the thermo-mechanical response of the fractured rock to the hot water injection.

The moment analysis results of the effects of hot water injection on fluid flow properties can also facilitate numerically quantifying the thermo-mechanical behavior of the test rock volume and the subsequent changes in permeability of the fracture network. We also showed a case of combining solute tracer concentration measurements with temperature perturbations to delineate fracture geometries, based on a simple single parallel plate model. Despite the simplicity of our model, further numerical studies, attempting to model the thermo-hydro-mechanical behavior of the study site, will likely benefit from the scoping calculations of the fracture geometries presented here. Finally, by conducting field-scale tracer experiments in hydraulically stimulated fractured crystalline rock, we provided insights into the evolution of fluid flow distribution and hydraulic connections during fluid circulation. Such processes may be critical during the operation of an actual EGS, as it is necessary to understand the induced changes in fluid flow geometry and rate, due to the injection of a fluid with a temperature that is different from the in situ rock temperature. With such understanding, one can better estimate the lifetime of fracture-dominated geothermal formations, such as EGS, from which geothermal energy is being produced.

Abbreviations

ϕ: Porosity (−); $\Phi(t)$: Storage capacity (−); ρ: Density (kg/m^3); A: Surface area (m^2); b: Aperture of the fracture (m); $C_{p,i}$: Heat capacity (i = water W, rock R) (J/kg/K); $E(t)$: Tracer residence time (1/s); $F(t)$: Flow capacity (−); G: Gini coefficient (−); K_R: Thermal conductivity of the rock (J/s/m/K); L: Fracture length (m); m_0^*: Zeroth temporal moment (−); m_1^*: First temporal moment (s); $m_{2,c}$: Second centralized and normalized temporal moment (s^2); M_{inj}: Mass of tracer injected (kg); q_{inj}: Volumetric injection rate (m^3/s); q_{pro}: Volumetric production rate (m^3/s); R: Recovery (%); S: Surface area of fracture (m^2); t: Time (s); t^*: Mean residence time (s); T_I: Initial temperature (°C); T_J: Injected temperature (°C); T_R: Temperature in the rock (°C); T_W: Temperature in the fracture (°C); V_p: Swept volume (m^3); W: Fracture width (m); z: Axis perpendicular to the fracture (m); DFN: Discrete fracture network; EGS: Enhanced geothermal systems; GPR: Ground penetrating radar; GTS: Grimsel test site; ISC: In situ stimulation and circulation; OPTV: Optical televiewer; RTD: Residence time distribution; THMS: Thermo-hydro-mechanical and seismic.

Acknowledgements

Authors' contributions

AK and MRJ planned the experiments and collected the data, AK performed the analytical calculations, interpreted the data and wrote the manuscript with support from XZK. MOS contributed to the design of the work and provided critical revision of the manuscript. All authors read and approved the final manuscript.

Funding

Availability of data and materials

The dataset supporting the conclusions of this article is available in the ETH Research Collection repository, https://www.research-collection.ethz.ch/handle/20.500.11850/348073.

Competing interests

The authors declare that they have no competing interests.

Author details

[1] Geothermal Energy and Geofluids Group, Department of Earth Sciences, ETH Zürich, Sonneggstrasse 5, Zürich 8092, Switzerland. [2] SCCER-SoE, ETH Zürich, Sonneggstrasse 5, Zürich 8092, Switzerland. [3] Department of Engineering Geology and Hydrogeology, RWTH Aachen, Aachen, Germany. [4] Department of Earth and Environmental Sciences, University of Minnesota, Minneapolis, USA. [5] Present Address: Geological Survey of Finland, Kuopio, Finland.

References

Amann F, Gischig V, Evans K, Doetsch J, Jalali R, Valley B, et al. The seismo-hydromechanical behavior during deep geothermal reservoir stimulations: open questions tackled in a decameter-scale in situ stimulation experiment. Solid Earth. 2018;9(1):115–37. https://doi.org/10.5194/se-9-115-2018.

Anderson MP. Heat as a ground water tracer. Ground Water. 2005;43(6):951–68. https://doi.org/10.1111/j.1745-6584.2005.00052.x.

André L, Rabemanana V, Vuataz FD. Influence of water–rock interactions on fracture permeability of the deep reservoir at Soultz-sous-Forêts; France. Geothermics. 2006;35(5–6):507–31.

Ayling BF, Hogarth RA, Rose PE. Tracer testing at the Habanero EGS site, central Australia. Geothermics. 2016;63:15–26.

Brixel B, Jalali M, Klepikova MV. Single- and cross-hole hydraulic characterization of the ISC support volume at the grimsel test site. ETH Research Collection; 2019. https://www.research-collection.ethz.ch/handle/20.500.11850/306205.

Brixel B, Klepikova M, Jalali MR, Lei Q, Roques C, Krietsch H, et al. Tracking fluid flow in shallow crustal fault zones: 1. Insights from single-hole permeability estimates. J Geophys Res Solid Earth. 2020a;. https://doi.org/10.1029/2019JB018200.

Brixel B, Klepikova M, Lei Q, Roques C, Jalali M, Krietsch H, et al. Tracking fluid flow in shallow crustal fault zones: 2. Insights from cross-hole forced flow experiments in damage zones. J Geophys Res Solid Earth. 2020b;. https://doi.org/10.1029/2019JB019108.

Carlslaw HS, Jaeger JC. Conduction of heat in solids. 2nd ed. Oxford: Clarendon Press; 1959.

Cirpka OA, Kitanidis PK. Characterization of mixing and dilution in heterogeneous aquifers by means of local temporal moments. Water Resour Res. 2000;5(36(5)):1221–36. https://doi.org/10.1029/1999WR900354.

Colombani N, Giambastiani BMS, Mastrocicco M. Combined use of heat and saline tracer to estimate aquifer properties in a forced gradient test. J Hydrol. 2015;525:650–7.

Danckwerts PV. Continuous flow systems. Chem Eng Sci. 1953;2(1):1–13.

de La Bernardie J, Bour O, Le Borgne T, Guihéneuf N, Chatton E, Labasque T, et al. Thermal attenuation and lag time in fractured rock: theory and field measurements from joint heat and solute tracer tests. Water Resour Res. 2018;54(12):053. https://doi.org/10.1029/2018WR023199.

de Marsily G. Quantitative hydrogeology: groundwater hydrology for engineers. Orlando: Academic; 1986.

Doetsch J, Gischig V, Krietsch H, Villiger L, Amann F, Dutler N, et al. Grimsel ISC Experiment Description. Zurich: SCCER-SoE; 2018. https://www.research-collection.ethz.ch:443/handle/20.500.11850/310581.

Evans KF. Reservoir creation. In: Hirschberg S, Wiemer S, Burgherr P, editors. Energy Earth. Zürich: vdf Hochschulverlag AG; 2015. p. 82–118.

Finsterle S, Zhang Y, Pan L, Dobson P, Oglesby K. Microhole arrays for improved heat mining from enhanced geothermal systems. Geothermics. 2013;47(July 2013):104–15. https://doi.org/10.1016/j.geothermics.2013.03.001.

Fu P, Hao Y, Walsh SDC, Carrigan CR. Thermal drawdown-induced flow channeling in fractured geothermal reservoirs. Rock Mech Rock Eng. 2016;49(3):1001–24.

Giambastiani BMS, Colombani N, Mastrocicco M. Limitation of using heat as a groundwater tracer to define aquifer properties: experiment in a large tank model. Environ Earth Sci. 2013;70(2):719–28. https://doi.org/10.1007/s12665-012-2157-2.

Giertzuch PL, Doetsch J, Jalali M, Shakas A, Schmelzbach C, Maurer H. High-resolution time-lapse GPR monitoring of saline tracer flow in fractured rock. In: Geophysical research abstracts. vol. 21. Vienna: EGU General Assembly 2019. 2019. p. 13983. https://meetingorganizer.copernicus.org/EGU2019/EGU2019-13983-1.pdf.

Gischig VS, Doetsch J, Maurer H, Krietsch H, Amann F, Evans KF, et al. On the link between stress field and small-scale hydraulic fracture growth in anisotropic rock derived from microseismicity. Solid Earth. 2018;9(1):39–61.

Gischig VS, Giardini D, Amann F, Hertrich M, Krietsch H, Loew S, et al. Hydraulic stimulation and fluid circulation experiments in underground laboratories: stepping up the scale towards engineered geothermal systems. Geomech Energy Environ. 2019;3:100175.

Grant MA. Physical performance indicators for HDR/EGS projects. Geothermics. 2016;63:2–4.

Grimm Lima M, Vogler D, Querci L, Madonna C, Hattendorf B, Saar MO, et al. Thermally driven fracture aperture variation in naturally fractured granites. Geotherm Energy. 2019;. https://doi.org/10.1186/s40517-019-0140-9.

Gringarten AC, Sauty JP. A theoretical study of heat extraction from aquifers with uniform regional flow. J Geophys Res. 1975;12(80(35)):4956–62. https://doi.org/10.1029/JB080i035p04956.

Guo B, Fu P, Hao Y, Peters CA, Carrigan CR. Thermal drawdown-induced flow channeling in a single fracture in EGS. Geothermics. 2016;61:46–62.

Hawkins AJ, Fox DB, Becker MW, Tester JW. Measurement and simulation of heat exchange in fractured bedrock using inert and thermally degrading tracers. Water Resour Res. 2017a;53(2):1210–30.

Hawkins AJ, Becker MW, Tsoflias GP. Evaluation of inert tracers in a bedrock fracture using ground penetrating radar and thermal sensors. Geothermics. 2017b;5(67):86–94.

Hawkins AJ, Becker MW, Tester JW. Inert and adsorptive tracer tests for field measurement of flow-wetted surface area. Water Resour Res. 2018;54(8):5341–58. https://doi.org/10.1029/2017WR021910.

Irvine DJ, Simmons CT, Werner AD, Graf T. Heat and solute tracers: how do they compare in heterogeneous aquifers? Groundwater. 2015;53(S1):10–20. https://doi.org/10.1111/gwat.12146.

Jalali MR, Gischig V, Doetsch J, Krietsch H, Amann F, Klepikova M. Mechanical, hydraulic and seismological behavior of crystalline rock as a response to hydraulic fracturing at the grimsel test site. In: Proceedings of 51st US rock mechanics/geomechanics symposium. San Francisco; 2017. p. 17–0962.

Jalali M, Gischig V, Doetsch J, Näf R, Krietsch H, Klepikova M, et al. Transmissivity changes and microseismicity induced by small-scale hydraulic fracturing tests in crystalline rock. Geophys Res Lett. 2018a;3(45(5)):2265–73. https://doi.org/10.1002/2017GL076781.

Jalali M, Klepikova M, Doetsch J, Krietsch H, Brixel B, Dutler N, et al. A multi-scale approach to identify and characterize preferential flow paths in a fractured crystalline rock. In: American rock mechanics association (ARMA). Seattle, USA; 2018b. p. 9.

Kant MA, Ammann J, Rossi E, Madonna C, Höser D, Rudolf von Rohr P. Thermal properties of central aare granite for temperatures up to 500°C: irreversible changes due to thermal crack formation. Geophys Res Lett. 2017;44:771–6.

Keusen HR, Ganguin J, Schuler P, Buletti M. Grimsel Test Site—-Geology. Baden: NAGRA; 1989. https://www.nagra.ch/data/documents/database/dokumente/default/DefaultFolder/Publikationen/NTBs 1987-1988/e_ntb87-14 E.pdf.

Kittilä A, Jalali MR, Evans KF, Willmann M, Saar MO, Kong XZ. Field comparison of DNA-labeled nanoparticle and solute tracer transport in a fractured crystalline rock. Water Resour Res. 2019;7(55(8)):6577–95. https://doi.org/10.1029/2019WR025021.

Kittilä A, Jalali M, Somogyvári M, Evans KF, Saar MO, Kong XZ. Characterization of the effects of hydraulic stimulation with tracer-based temporal moment analysis and tomographic inversion. Geothermics. 2020;86:101820. https://doi.org/10.1016/j.geothermics.2020.101820.

Kocabas I. Geothermal reservoir characterization via thermal injection backflow and interwell tracer testing. Geothermics. 2005;34(1):27–46.

Kolditz O. Modeling flow and heat-transfer in fractured rocks - conceptual model of a 3-D deterministic fracture network. Geothermics. 1995;24(3):451–70.

Kong XZ, Deuber CA, Kittilä A, Somogyvári M, Mikutis G, Bayer P, et al. Tomographic reservoir imaging with DNA-labeled silica nanotracers: the first field validation. Environ Sci Technol. 2018;52(23):13681–9. https://doi.org/10.1021/acs.est.8b04367.

Krietsch H, Doetsch J, Dutler N, Jalali M, Gischig V, Loew S, et al. Comprehensive geological dataset describing a crystalline rock mass for hydraulic stimulation experiments. Sci Data. 2018;11(5):12.

Krietsch H, Gischig V, Evans K, Doetsch J, Dutler NO, Valley B, et al. Stress measurements for an in situ stimulation experiment in crystalline rock: integration of induced seismicity, stress relief and hydraulic methods. Rock Mechanics Rock Eng. 2019;52(2):517–42. https://doi.org/10.1007/s00603-018-1597-8.

Kumari WGP, Ranjith PG, Perera MSA, Chen BK. Experimental investigation of quenching effect on mechanical, micro-structural and flow characteristics of reservoir rocks: thermal stimulation method for geothermal energy extraction. J Petrol Sci Eng. 2018;162:419–33.

Lauwerier HA. The transport of heat in an oil layer caused by the injection of hot fluid. Appl Sci Res. 1955;5(2–3):145–50. https://doi.org/10.1007/BF03184614.

Leube PC, Nowak W, Schneider G. Temporal moments revisited: why there is no better way for physically based model reduction in time. Water Resour Res. 2012;48(11):W11527. https://doi.org/10.1029/2012WR011973.

Linde N, Finsterle S, Hubbard S. Inversion of tracer test data using tomographic constraints. Water Resour Res. 2006;42(4):1–15.

Luhmann AJ, Covington MD, Myre JM, Perne M, Jones SW, Alexander EC Jr, et al. Thermal damping and retardation in karst conduits. Hydrol Earth Syst Sci. 2015;19:137–57.

Ma R, Zheng C, Zachara JM, Tonkin M. Utility of bromide and heat tracers for aquifer characterization affected by highly transient flow conditions. Water Resour Res. 2012;. https://doi.org/10.1029/2011WR011281.

Marschall P, Vomvoris S, Bossart P, Correa N, Guyonnet D, Heinemann-Glutsch B, et al. Developments in hydrotesting, fluid logging and combined salt/heat tracer experiments in the BK site (phase III). Wettingen: Nagra; 1995. p. NTB 93.

McCord J, Reiter M, Phillips F. Heat-flow data suggest large ground-water fluxes through Fruitland coals of the northern San Juan basin. Colorado-New Mex Geol. 1992;20(5):419–22.

Mikutis G, Deuber CA, Schmid L, Kittilä A, Lobsiger N, Puddu M, et al. Silica-encapsulated DNA-based tracers for aquifer characterization. Environ Sci Technol. 2018;52(21):12142–52. https://doi.org/10.1021/acs.est.8b03285.

National research council. Rock fractures and fluid flow: contemporary understanding and applications. Washington, DC: The National Academies Press; 1996. https://www.nap.edu/read/2309/chapter/1.

Olasolo P, Juárez MC, Morales MP, Damico S, Liarte IA. Enhanced geothermal systems (EGS): a review. Renew Sustain Energy Rev. 2016;56:133–44. https://doi.org/10.1016/j.rser.2015.11.031.

Pandey SN, Chaudhuri A, Kelkar S. A coupled thermo-hydro-mechanical modeling of fracture aperture alteration and reservoir deformation during heat extraction from a geothermal reservoir. Geothermics. 2017;65:17–31.

Rau GC, Andersen MS, Acworth RI. Experimental investigation of the thermal dispersivity term and its significance in the heat transport equation for flow in sediments. Water Resour Res. 2012;48:W03511. https://doi.org/10.1029/2011WR011038.

Robinson BA, Tester JW. Dispersed fluid flow in fractured reservoirs: an analysis of tracer-determined residence time distributions. J Geophys Res. 1984;89(B12):10374–84. https://doi.org/10.1029/JB089iB12p10374.

Rutqvist J, Börgesson L, Chijimatsu M, Nguyen TS, Jing L, Noorishad J, et al. Coupled thermo-hydro-mechanical analysis of a heater test in fractured rock and bentonite at Kamaishi Mine—comparison of field results to predictions of four finite element codes. Int J Rock Mech Min Sci. 2001;38(1):129–42.

Saar MO. Review: geothermal heat as a tracer of large-scale groundwater flow and as a means to determine permeability fields. Hydrogeol J. 2011;19(1):31–52.

Sarris TS, Close M, Abraham P. Using solute and heat tracers for aquifer characterization in a strongly heterogeneous alluvial aquifer. J Hydrol. 2018;558:55–71.

Shook GM. A simple, fast method of estimating fractured reservoir geometry from tracer tests. Geotherm Resour Counc Trans. 2003;27:407–11.

Shook GM, Forsmann JH. Tracer interpretation using temporal moments on a spreadsheet. Idaho National Laboratory; 2005. https://inldigitallibrary.inl.gov/sites/sti/sti/3028333.pdf.

Shook GM, Suzuki A. Use of tracers and temperature to estimate fracture surface area for EGS reservoirs. Geothermics. 2017;67:40–7.

Somogyvári M, Bayer P. Field validation of thermal tracer tomography for reconstruction of aquifer heterogeneity. Water Resour Res. 2017;53(6):5070–84. https://doi.org/10.1002/2017WR020543.

Somogyvári M, Bayer P, Brauchler R. Travel-time-based thermal tracer tomography. Hydrol Earth Syst Sci. 2016;20(5):1885–901.

Taron J, Elsworth D. Thermal-hydrologic-mechanical–chemical processes in the evolution of engineered geothermal reservoirs. Int J Rock Mech Min Sci. 2009;46(5):855–64.

Tester JW, Anderson BJ, Batchelor AS, Blackwell DD, DiPippo R, Drake EM, et al. The Future of geothermal energy: impact of enhanced geothermal systems (EGS) on the United States in the 21st century. Cambridge: Massachusetts Institute of Technology; 2006. INL/EXT-06-11746. http://www.eere.energy.gov/geothermal/pdfs/structure_outcome.pdf.

Wenning Q, Madonna C, de Haller A, Burg JP. Permeability and seismic velocity anisotropy across a ductile-brittle fault zone in crystalline rock. Solid Earth. 2018;9:683–98.

Yasuhara H, Kinoshita N, Ohfuji H, Lee DS, Nakashima S, Kishida K. Temporal alteration of fracture permeability in granite under hydrothermal conditions and its interpretation by coupled chemo-mechanical model. Appl Geochem. 2011;26(12):2074–88.

Ziegler M, Loew S, Moore JR. Distribution and inferred age of exfoliation joints in the Aar Granite of the central Swiss Alps and relationship to Quaternary landscape evolution. Geomorphology. 2013;11(201):344–62.

Publisher's Note

Springer Nature remains neutral with regard to jurisdictional claims in published maps and institutional affiliations.